Contents lists available at ScienceDirect

# Composites Science and Technology

journal homepage: http://www.elsevier.com/locate/compscitech

# Personalized 4D printing of bioinspired tracheal scaffold concept based on magnetic stimulated shape memory composites

Wei Zhao [a], Fenghua Zhang [b], Jinsong Leng [b], Yanju Liu [a],*

[a] Department of Astronautical Science and Mechanics, Harbin Institute of Technology (HIT), P.O. Box 301, No. 92 West Dazhi Street, Harbin, 150001, People's Republic of China
[b] National Key Laboratory of Science and Technology On Advanced Composites in Special Enviroments, Harbin Institute of Technology (HIT), No.2 Yikuang Street, P.O. Box 3011, Harbin, 150080, People's Republic of China

## A B S T R A C T

Shape memory polymers (SMPs) can be triggered by an external stimulus to realize the shape changing from temporary shape to its original shape. Due to its biodegradability, easy forming properties and shape memory effect, SMPs have been widely considered in bio-medical applications. This paper details an application of SMP in personalized 4D printing of a bio-designed tracheal scaffold. Compared with the traditional tracheal scaffolds, the SMP tracheal scaffolds can conform to the issue to keep the best fixed state. Moreover, the design of tracheal scaffold based on the microstructure of the glass sponge exhibits higher strength and stability. The distinctive design endows it with the ability to adapt the complex environmental conditions in the soft-tissue of patients. Combined with 4D printing, the bioinspired tracheal scaffold can realize customization in consideration of different size of trachea. The SMP based bio-designed tracheal scaffolds showed excellent performances and were proved to be a potential replacement for the traditional tracheal scaffold.

## 1. Introduction

As air conduit, trachea has the function of providing warm, humid and clean air for respiratory zone, clearing secretions and keeping the airway free [1]. Many of the flexible tracheas and tubules together constitute the tracheobronchial tree, which is approximately 12 cm long with 2 cm diameter in the body. Usually, trachea is fragile, so that it can be impaired by many disorders [2–4]. And air conduit is a single intraluminal organ with independent biological characteristics and functions. Owing to its unique anatomical structure, the surgical repair of damaged trachea is very complicated and accompanied with high risks [5–8]. Adopting the artificial tracheal scaffold repair method will relieve pain. With the development and maturity of the biomedical technology, more and more excellent tracheal scaffolds have been developed, especially by using the degradable scaffold materials [1,9].

Tracheal scaffold is the medical device used to repair tracheal stenosis and tracheomalacia. Currently, most of the tracheal scaffolds used in clinical researches are non-degradable. However, with the developments of biodegradable materials, more and more studies are focused on the biodegradable tracheal scaffold [9,10]. It can provide mechanical support for tracheal wall in the initial stage. After the

growth of the cell tissue along the scaffold wall, it can degraded and excreted outside gradually, avoiding the re-injury caused by the second operation [11].

Unfortunately, frequent complications usually cause faults, such as scaffold migration and scaffold fracture [12]. Thus, it is necessary that the tracheal scaffold must have enough mechanical strength and good bending performance. Most importantly, it must fit the trachea ideally to avoid sliding. Thus, motivated by the high risk of the failure and migration of the implanted tracheal scaffold, the personalized four-dimensional (4D printing) of bioinspired tracheal scaffold based on shape memory polymer (SMPs) is engineered with adaptive design, which can fit the trachea ideally and provide a conformable fixation.

4D printing is developed based on the 3D printing (three-dimensional printing) technology, or additive manufacturing technology, with the usage of some special features of intelligent materials, like shape memory polymer. Shape memory polymer can respond to external stimulus (such as electricity [13], light [14], magnetism [15], water [16], heat [17] and microwave [18]) under specific conditions and capable of self-sensing, self-actuation, self-drive and self-healing. Due to its special functions, SMP have been widely used in the fields such as aerospace [19–21], adaptive optics [22,23], biomedical [24,25], and
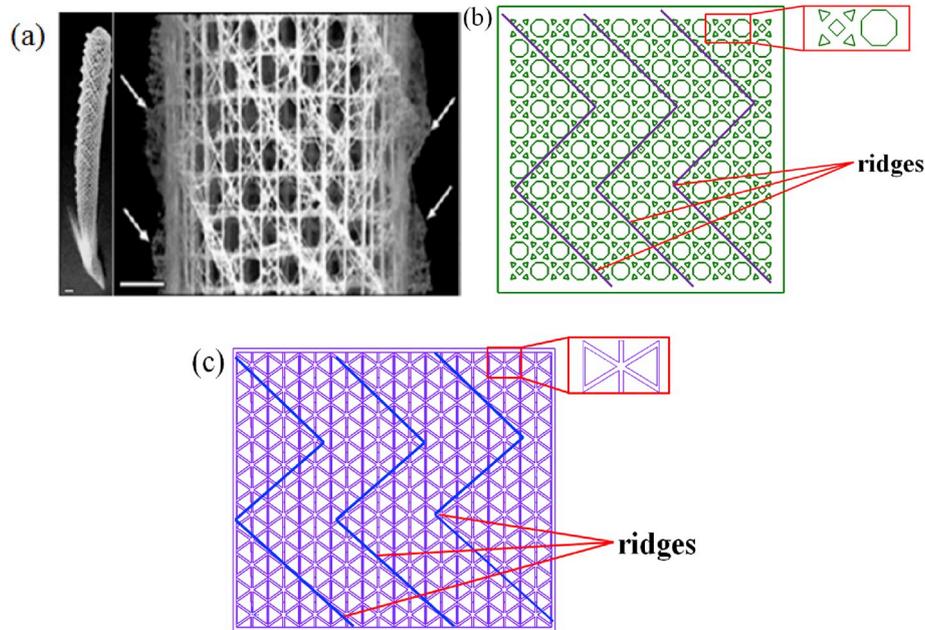
---

**Fig. 1.** (a) Photograph of the entire skeleton of a glass sponge and the fragment of the cage structure (b) Plane graph of the deployable structure and cell-element of bioinspired tracheal scaffold BTS-I and (c) BTS-II.

etc. The additive manufacturing technology of SMP has overcome the disadvantage in traditional SMP fabrication technology. Fabrication of structures with complex shapes is not easy to achieve, but additive manufacturing makes it possible to prepare structures with arbitrarily complex shape, which further expands the application scope of SMP, especially in biomedical area. Jia et al. detailed the application of additive manufacturing technology in surgical practices [26]. Zhang et al. pointed out that the importance of the additive manufacturing technology to personalized designs, and discussed the improvement project of additive manufacturing technology to achieve desired bio-functionality [27].

4D printing can be used in multiple biomedical applications, ranging from the design of nanoparticle to the fabrication of engineering scaffold, based on shape memory biomedical materials [28–30]. Due to the tiny structure can be implanted into the limited access places and then be expanded, 4D printing has a great potential in the biomedical applications. A bioinspired tracheal scaffold can be delivered to the lesion place, and recover to its permanent shape under the external stimulus. Wei et al. have processed several 4D scaffolds based on direct-write fabrication, which exhibit the potential in intravascular scaffold [31]. However, this work just reveal that the 4D printing technology has the potential for further development of biomedical application. The structure related in this paper is just used to shown its shape memory effect, which is not discussed in depth. Based on 4D printing technology, Zhang et al. have designed and fabricated a circular braided tube. The shape memory behavior and recovery force were characterized in their work [32].

Based on the additive manufacturing technology of intelligent materials, the process to achieve 4D printed components is described as follows. Firstly, the rapid manufacturing of SMP is realized by the additive manufacturing technology. Then under the external stimulation of the environment (light, electricity, humidity, temperature, etc.), the structure changes its initial state, providing the additional dimension of time, which is very suitable for the implantation of tracheal scaffold.

The structure configuration and holes size play an important role in the design of a tracheal scaffold. The suitable size of holes facilitates the attachment and growth of cell tissue on scaffold. Also a reasonable structural design determines the structural stability of the scaffold. Excellent mechanical stability of tracheal scaffold is expected to support

the softened tracheal besides providing support for cells. Thus, the following mechanical properties are required for an excellent tracheal scaffold. (i) After implanted in vivo, it must maintain the structural integrality and stability. (ii) It must provide sufficient force during the tissue regeneration and material degradation. This paper presents two bioinspired tracheal scaffolds with optimal holes size and high supporting capacity. Furthermore, the performances of the novel tracheal scaffolds are evaluated.

## 2. Design and fabrication of bioinspired tracheal scaffold

### 2.1. Design of porous glass sponge biomimetic tracheal scaffold

In order to adapt to their living environment, each species in nature has undergone a long natural selection and evolved to form a biological structure with excellent properties, such as high strength, high tenacity, self-sealing and good functional adaptability [33,34]. The best optimization design is successfully achieved in the existing structure of biological materials, such as bone, plant stem and wood fiber, which shows excellent performance in the direction of payload. Such mechanism is imitated by a variety of weaving methods [35]. The optimized arrangement of fibers found in biological structure can be applied to the stent for load-bearing [36]. Sandwich plate structures that imitate honeycomb structure have been extensively employed in the aerospace field. Taking the advantages into account, many biomimetic studies have been carried out.

The unique porous network structure of the glass sponge can satisfy some requirements of tracheal stent. Glass sponge is a type of spongy animal, and the skeleton is made of siliceous bone needles, which are similar to the composition of fiberglass and thus give it the name of glass sponge [37–39]. The complex biological environment of the seafloor resulted in their high toughness, high strength and high stability. The personalized 4D printing of bioinspired tracheal scaffold is simplified and designed on the basis of microstructure of porous glass sponge. The body wall of the porous glass sponge is cylindrical. It is composed of interweaving meridional circulation sponge spicule, zonal sponge spicule and spiral sponge spicule, which form the unique octagon mesh structure [40]. The serrations outside of the external wall of porous glass sponge are called external ridges, which extend perpendicularly to the
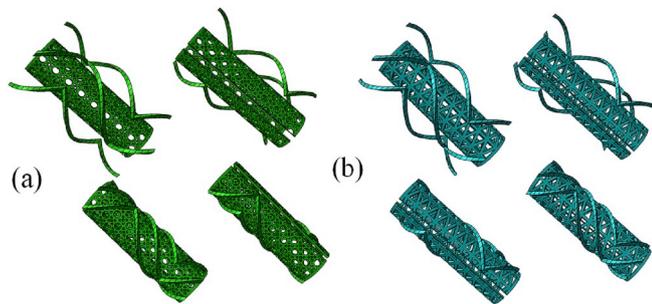
**Fig. 2.** Three-dimensional exploded-views and glass sponge inspired designs of tracheal scaffold of (a) BTS-I and (b) BTS-II.
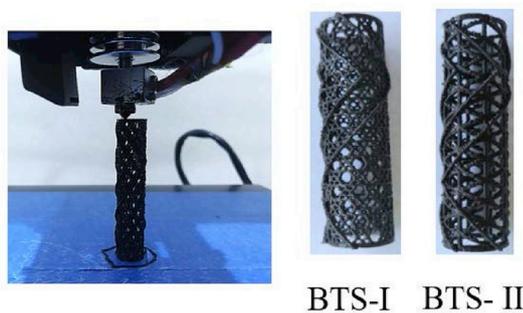


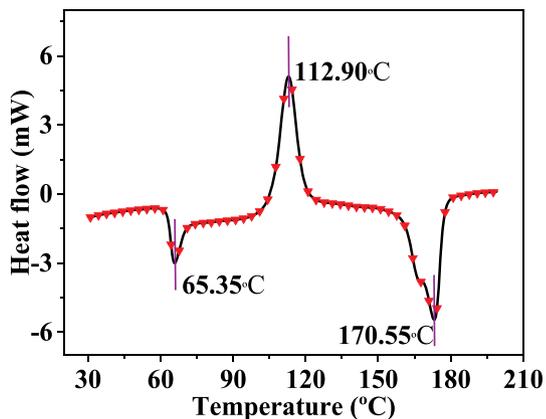**Fig. 3.** 4D Printing of bioinspired tracheal scaffold concept BTS-I and BTS- II.



**Fig. 4.** Differential scanning calorimetry curve.

surface of the body wall and spiral at an angle of 45°. Ridges provide support to backbone and improve the ability to withstand bending, shear and torsion. The skeleton of porous glass sponge is composed of fibers in four directions, 0°, 90° and ±45°.

Because of the special physiological characteristics of the trachea, particular demands in the geometrical shape, porosity and mechanical properties of the trachea scaffold are supposed to be considered. The configuration design of bioinspired tracheal scaffold is carried out based on the unique microstructure of porous glass sponge.

Fig. 1(a) exhibits a photograph of the entire skeleton of a glass sponge and the fragment of the cage structure. Inspired by this structure, two bioinspired tracheal scaffolds named as BTS-I and BTS- II are designed, and the plane graphs of the deployable structures are shown in Fig. 1(b) and (c) respectively. The outer wall of glass sponge is covered with the bidirectional spiral ridges, with (helical) angle of 45°, which are 0.4 mm high and 0.4 mm thick. The helical angle of the spiral ridges of glass sponge is inverted after a corresponding circumferential angle of π. The plane structure of bioinspired tracheal scaffold is composed by ±

45° crossed fiber. To reduce the weight of the scaffold, triangular and rectangular holes are scattered on the fibers. The main function of tracheal scaffold is to provide mechanical support for the lesion site. Also, the mechanical properties of trachea scaffold could be maintained by controlling the porosity and pore size. The enlarged view of the cellular elements of the porous structure of BTS-I is illustrated in Fig. 1 (b). Accordingly, the triangular holes are radially distributed around the rectangles. The cellular elements array along the fiber directions and the octagonal holes lie on the junction of the fiber. As shown in Fig. 1 (c), the cellular elements of the BTS-II array along the fiber directions and lie on both side of the fiber.

Fig. 2 (a) illustrates the three-dimensional exploded-views and complete glass sponge inspired design of bioinspired tracheal scaffold BTS-I. It is composed of a skeleton in the center and ridges spiral around the wall. Similarly, Fig. 2 (b) shows the configuration of bioinspired tracheal scaffold BTS-II. The ratio between strength and weight is used to evaluate the performance of the designed scaffolds. The design criteria are shown in Appendix A.

### 2.2. Fabrication of shape memory PLA/Fe$_3$O$_4$ composites filament and bioinspired tracheal scaffold

With the increase of magnetic particle content, the heating efficiency will increase. However, if it has too few magnetic particles, the material could not be actuated due to the low concentration of magnetic particles (fewer induction heaters). It is found that when the content of the magnetic particle is lower than 5 wt%, it is hard to actuated. When the content of magnetic particles increased to 10 wt%, the sample was able to actuate the recovery process, but the recover speed is relatively lower. Consequently, the ratio of 15 wt% is chosen in this work.

The raw materials were processed by solvent. A masterbatch, containing 15 wt% Fe$_3$O$_4$ nanoparticles and 85 wt% polylactic acid (PLA) was first prepared by melt compounding. A twin-screw extruder (Cte20 Coperion) equipped with a sharp-shearing extruder screw (screw diameter: 24 mm, L/D ratio: 40) was employed for the preparation of the filament. The screw speed was set to 200 rpm, and the processing temperatures were ranged from 180 to 200 °C. The filament of shape memory PLA/Fe$_3$O$_4$ composites was wound around a spool while being extruded. The average filament diameter was 1.75 mm.

Model of the bioinspired tracheal scaffold used for 3D printing was created by using the Solidworks software package. Using the shape memory PLA/Fe$_3$O$_4$ filament, the tracheal scaffold was printed by fused deposition method with 20% infill density. The commercial 3D printer of ANYCUBIC 3D (i3 MEGA) with the nozzle size of 0.4 mm was employed to fabricate the scaffolds. The printing speed was set as 50 mm/min with the printing temperature of 210 °C and bed temperature of 60 °C. The prototypes of BTS-I and BTS-II are shown in Fig. 3. The heights of the scaffolds were 50 mm and the diameters were 12 mm. The wall thickness of the scaffold was 0.8 mm and the protruding height of three external ridges was 0.4 mm, which were designed to improve the strength and toughness of the structure.

### 3. Experimental methods and results

#### 3.1. Thermodynamic experiment

##### 3.1.1. Differential scanning calorimetry (DSC)

Differential scanning calorimetry (DSC 1 STAR System, Mettler-Toledo) test was performed to investigate its thermodynamic performance. The sample was heated to 200 °C with a rate of 10 °C/min and cooled to 30 °C with the same rate. As shown in Fig. 4, the glass transition temperature is 65.35 °C and the melting temperature is 170.55 °C. However, there is a cold crystal peak around 110 °C, which indicates that PLA is semi-crystalline material with weak crystallization ability.
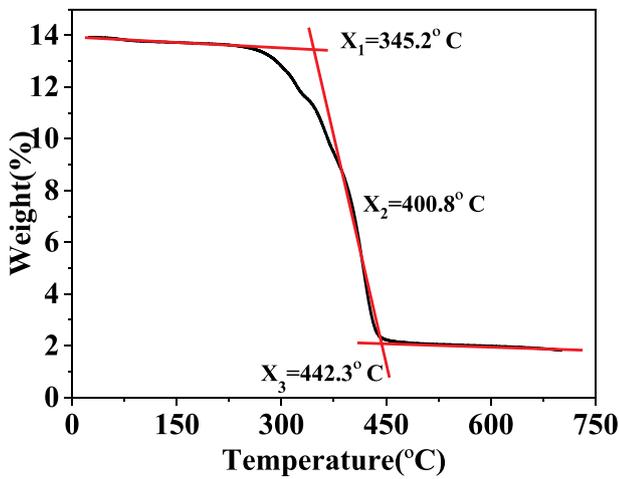
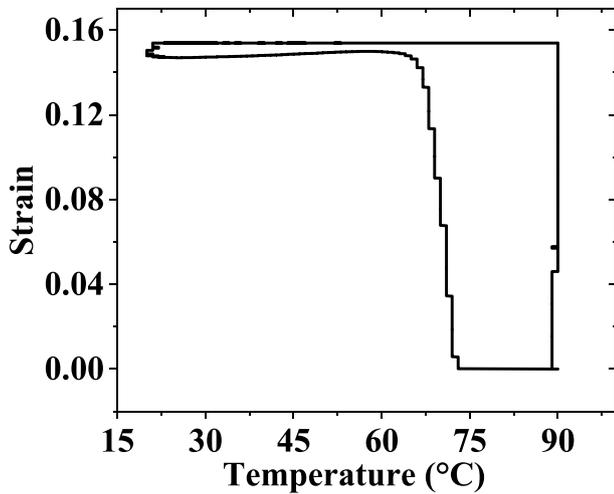**Fig. 5.** Thermogravimetric analysis curve.



**Fig. 6.** Shape memory cycle of strain vs. temperature.

### 3.1.2. Thermogravimetric analysis (TGA)

Thermogravimetric analysis (TGA/DSC 1 STAR System, Mettler-Toledo) was performed with a heating rate of 10 °C/min, which the sample was heated from 25 °C to 700 °C. The tendency of material decomposition is shown in Fig. 5. The temperature where $PLA/Fe_3O_4$ is completely decomposed is around 440 °C with the residual mass of 1.91 mg. Furthermore, it can be obtained that the initial thermal

decomposition temperature is 345.2 °C ($X_1$), the temperature with the highest thermal decomposition rate is 400.8 °C ($X_2$) and the end thermal decomposition temperature is 442.3 °C ($X_3$).

### 3.1.3. Thermal-mechanical cycle test

Thermal-mechanical test is conducted to investigate the shape memory effect of the $PLA/Fe_3O_4$ composites. The sample is first heated to 90 °C with the heating rate of 2 °C/min and applied 0.15 strain. Keep the strain and lower the temperature to 20 °C with the cooling rate of
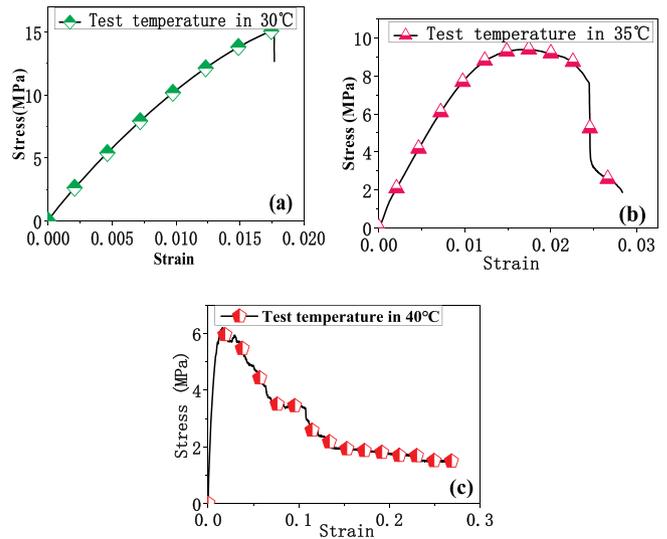


**Fig. 8.** Uniaxial tensile test of $PLA/Fe_3O_4$ composite at (a) 30 °C (b) 35 °C (c) 40 °C.
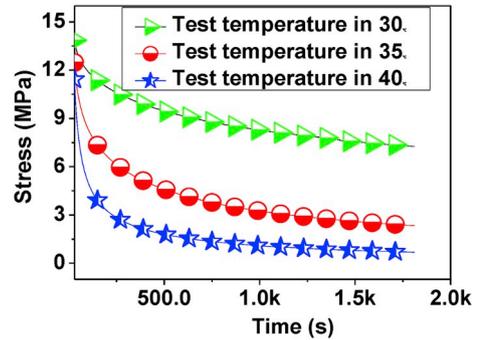


**Fig. 9.** Stress relaxation test of $PLA/Fe_3O_4$ composite at 30 °C, 35 °C and 40 °C.
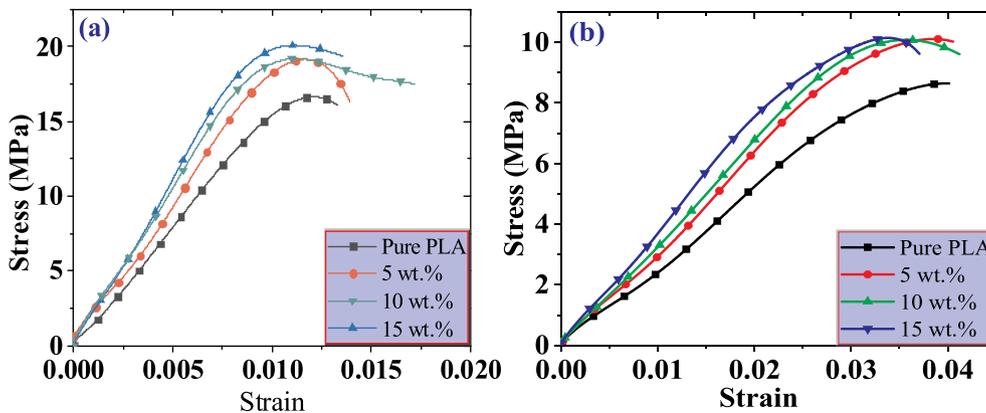


**Fig. 7.** Uniaxial tensile experiments of samples with different particle content (a) Test temperature in 25 °C (b) Test temperature in 37 °C.
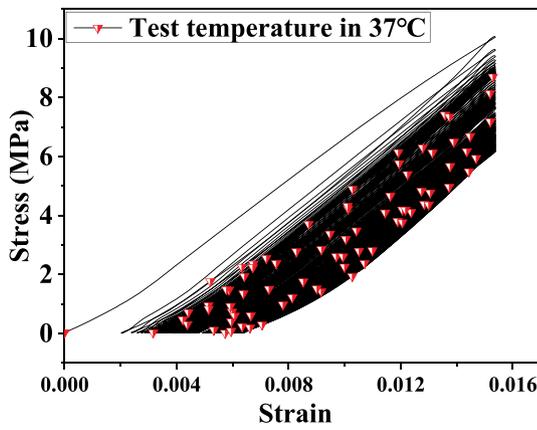
**Fig. 10.** Durability test curve of PLA/Fe$_3$O$_4$ composite.

2 °C/min. Finally, reheat the sample to 90 °C with the same heating rate. As shown in Fig. 6, it can be seen that the sample starts to recover its initial shape around 60 °C, and the recover speed is relatively fast. When the temperature reaches to 73 °C, the sample has finished its thermal-mechanical process. This test, from the side, reflects the recovery of the scaffold. However, the thinner wall of the scaffold will result in heat conduction faster than the sample, which will further lead to the recover temperature of the scaffold lower than the sample and the recover speed higher than the sample.

### 3.2. Uniaxial tensile test

The tensile tests were performed according to ASTM D638 standard by using a universal testing machine (ZWICK-010) equipped with a temperature chamber. Dumbbell-shaped samples with a filling rate of 20% were prepared by using 3D printer, and the size was 115 mm × 6 mm × 2 mm. Before testing, the specimen was put inside the temperature chamber to stabilize for 15 min to achieve the thermal

equilibrium. The stretching speed was controlled at 2 mm/min.

Samples of pure PLA and PLA/Fe$_3$O$_4$ (PLA mixed with 5 wt%, 10 wt% and 15 wt% Fe$_3$O$_4$) were adopted to explore the influence caused by the addition of magnetic particle on mechanical properties. Moreover, two groups of experiments were carried out with test temperature of 25 °C and 37 °C to study the stress-strain behavior under different temperature. The stress-strain behavior tested at 25 °C is shown in Fig. 7 (a). Obviously, the mechanical strength of PLA mixed with 15 wt% Fe$_3$O$_4$ is the highest among the four materials, which is 20.08 MPa and much higher than 16.63 MPa of pure PLA. Moreover, the mechanical strengths of PLA mixed with 10 wt% and 5 wt% Fe$_3$O$_4$ are 19.19 MPa and 19.10 MPa, which is slightly less than that of PLA mixed with 15 wt% Fe$_3$O$_4$, but both are higher than pure PLA. The stress-strain behavior
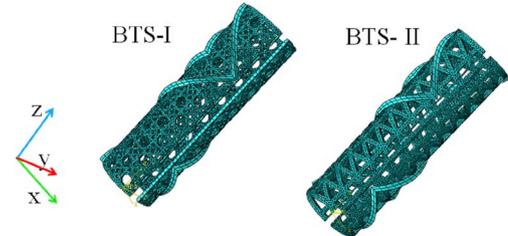


**Fig. 12.** The initial configuration of bioinspired tracheal scaffold BTS-I and BTS-II after imported into ABAQUS.

**Table 1**
Parameters of the applied constitutive model.

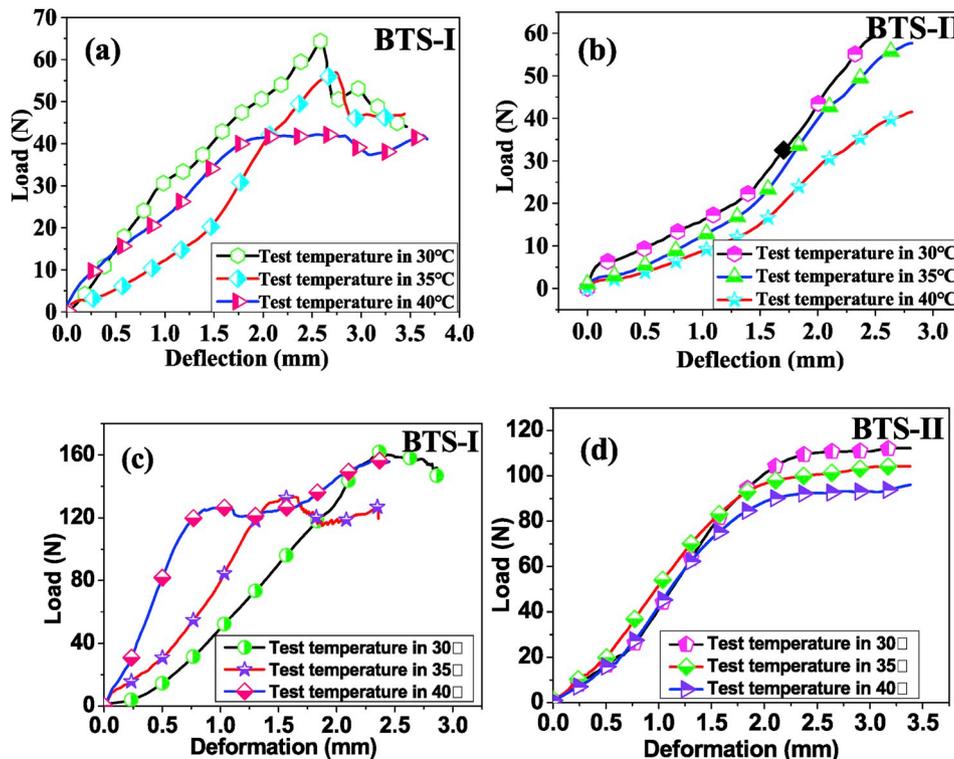| Description | Parameter | Values |
| --- | --- | --- |
| Hyperelastic parameters | $C_{10}$, $D_1$ | 393.964, 0.0006452 |
| Thermal expansion coefficient | a | 0.00017 (at 40 °C) |
| WLF reference temperature | $T_0$ | 37 °C |
| WLF constant | $C_1$ | 4.5 |
| WLF constant | $C_2$ | 55 |



**Fig. 11.** Three-point bending test results of bioinspired tracheal scaffold (a) BTS-I and (b) BTS-II, Radial strength test curves of (c) BTS-I and (d) BTS-II.
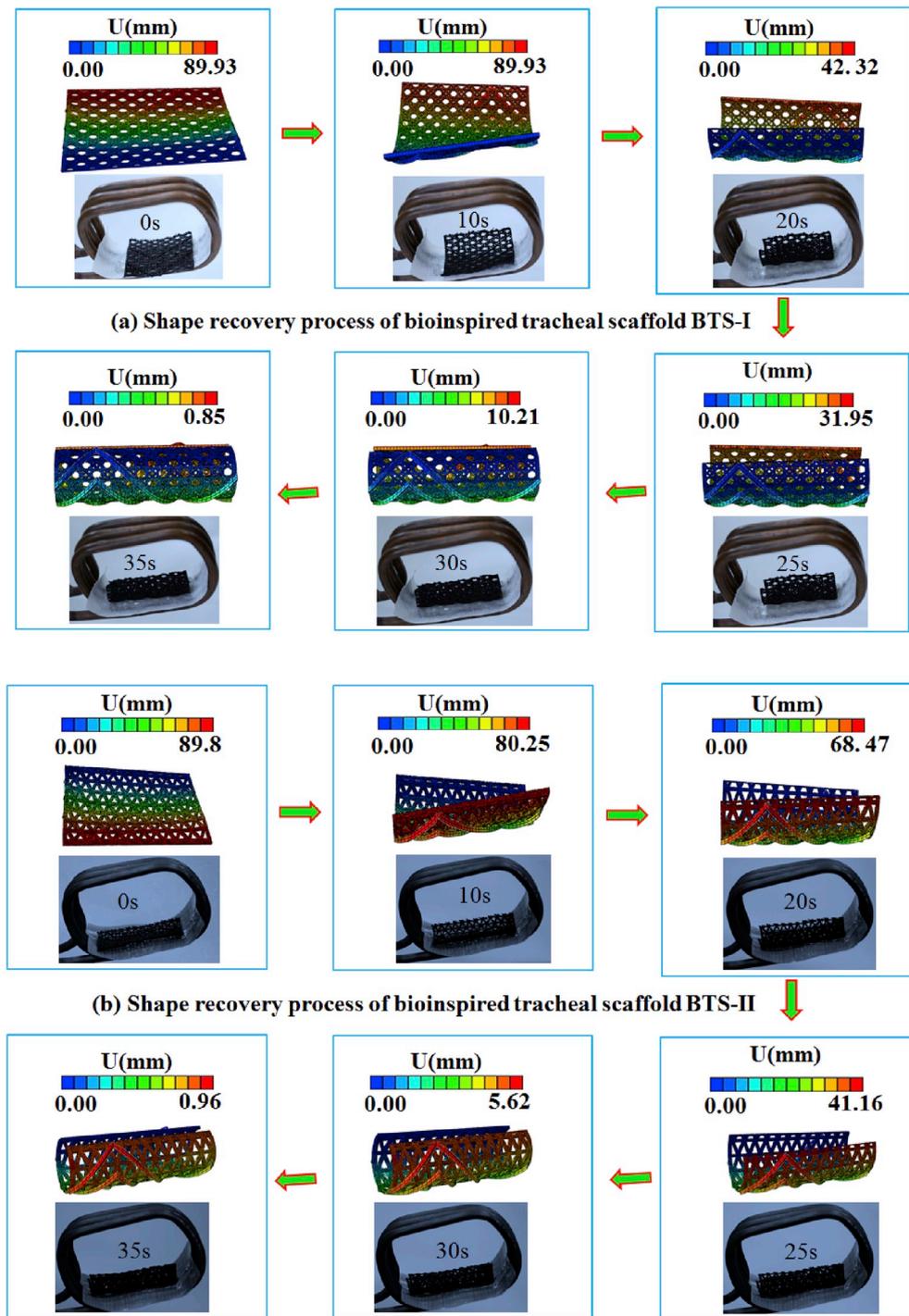
**Fig. 13.** Function verification of bioinspired tracheal scaffold (a) BTS-I and (b) BTS- II in vitro actuated by magnetic field.

tested at 37 °C is shown in Fig. 7(b). The mechanical strength of PLA/Fe$_3$O$_4$ with 15 wt%, 10 wt% and 5 wt% Fe$_3$O$_4$ is 10.14 MPa, 10.07 MPa and 10.09 MPa, which is significantly higher than 8.64 MPa of pure PLA. Furthermore, as shown in Table F1 and Table F2 (Appendix F), the Young's modulus of PLA/Fe$_3$O$_4$ are significantly higher than pure PLA.

Consequently, it can be concluded that a certain amount of Fe$_3$O$_4$ has some enhancement effect on mechanical strength of PLA. The mechanical strength of PLA/Fe$_3$O$_4$ will be significantly improved compared with pure PLA. However, the difference of mechanical strength between PLA/Fe$_3$O$_4$ with different content of Fe$_3$O$_4$ is not obvious. Furthermore, the elastic modulus increases with the increasing of mass fraction of Fe$_3$O$_4$.

In order to obtain the mechanical properties of shape memory PLA/Fe$_3$O$_4$ composite, the uniaxial tensile test was conducted at three different temperatures close to body temperature (30 °C, 35 °C and 40 °C). As shown in Fig. 8, the specimens exhibit an excellent toughness around the body temperature. Besides, the Young's moduli calculated are 1293 MPa at 30 °C, 1039 MPa at 35 °C and 956 MPa at 40 °C. The mechanical strengths are 15.15 MPa at 30 °C, 9.39 MPa at 35 °C and 6.20 MPa at 40 °C while the fracture strains are 0.0176, 0.0283 and 0.27 at 30 °C, 35 °C and 40 °C, respectively. Consequently, it can be concluded that the Young's modulus and mechanical strength decrease with the increase of test temperature.

## 3.3. Relaxation test

The stress relaxation test is an important experimental method to investigate the viscoelastic mechanical property of SMP. By relaxation test, it can be found that the flow deformation of a SMP consists of two stages. Firstly, there is an instantaneous elastic deformation at the beginning of loading and then there is a viscous deformation at the end where the stress decays. The stress relaxation test was used to study the decay of stress $\sigma_0(t)$ under a constant strain. In this work, the deformation was kept at 1 mm and stress relaxation has been investigated at three temperatures 30 °C, 35 °C and 40 °C as shown in Fig. 9.

## 3.4. Durability test

In order to investigate the durability of the material, the cyclic loading-unloading measurement is carried out. The specimen used in this test is according to the same standard (ASTM D638, 11 5 mm × 6 mm × 2 mm). It is heated to 37 °C and kept for 15 min to ensure sufficient heat exchange. Subsequently, the sample is applied 1 mm deformation on it. When the load reaches to the maximum, it will be unloaded until zero. The cyclic process proceeds for 100 times, which indicate the excellent durability of the material. The experiment result is shown in Fig. 10.

## 3.5. Stability and radial strength test of bioinspired tracheal scaffold

The bioinspired tracheal scaffold should have excellent stability and radial strength to support the tracheal well. Meanwhile, the scaffold is supposed to deform slightly and recover quickly to adapt the deformation of the trachea caused by cough and breathe. During eating, coughing and breathing, the trachea will get squeezed to realize the in and out of gas and liquid discharging. Special mechanical properties of the tracheal scaffold can ensure the quick recovery to the initial state while providing the required mechanical support. Radial loading bearing capacity is one of the most important parameters of tracheal scaffold. During its development and clinical application, one of the main causes for failure is its collapse, which attributes to the insufficient radial strength. The failure of the tracheal scaffold inside the body will result in great pain for patients, or even life-threat. Thus, excellent mechanical properties of scaffolds are very important.

Multiple experiments are conducted in this work to evaluate the stability of tracheal scaffold in complex working environment. The three-point bending test is carried out at 30 °C, 35 °C and 40 °C respectively with a loading rate of 2 mm/min. The span was 35 mm while the length of the tracheal scaffold is 50 mm. As shown in Fig. 11(a) and (b), the tracheal scaffolds BTS-I and BTS-II have high resistance to

010 machine. And the compression mode is adopted with the loading rate of 2 mm/min. As showed in Fig. 11 (c) and (d), even at the temperature of 40 °C, the bioinspired tracheal scaffolds still exhibit an excellent radial strength.

From the experiment results of scaffolds BTS-I and BTS-II, it can be seen that the BTS-II is more stabilizing when subjected to different temperature environment compared to BTS-I. This maybe results from the different microstructures of the two structures. As shown in Fig. 2, triangular, rectangular and octagon holes are scattered on the fibers of scaffold BTS-I. However, the cellular elements of the BTS-II array along the fiber directions are the triangular holes. The stability of triangular elements results in the BTS-II exhibits better stability.

Quantitative data on the biomechanical properties of tracheobronchial stents is very complex and elusive. However, a relevant summary based on the animal experiment is provided in the supporting information published by Morrison et al. [9]. Eventually, the scaffold must provide adequate mechanical support to prevent the compressive force coming from external, while, some bending freedom is necessary. It can be quantified as < 50% deformation under a compressive load of 20 N [9]. By comparing the relation between the load and the deformation, the deformation under 20N of the bioinspired tracheal scaffold designed in our work is around 10%.

## 4. Constitutive modeling of SMPs

The viscoelastic constitutive model of finite deformation in transient response mode can be expressed as:

$$\tau_0(t) = \tau_0^D(\overline{F}(t)) + \tau_0^B(t) \tag{1}$$

where, $\tau_0^D$ and $\tau_0^B(t)$ are the partial and spherical portions of Kirchhoff stress $\tau_0$. And $\overline{F}$ is a variable associated with the deformation gradient $F$:

$$\overline{F} = \frac{F}{J^{\frac{1}{3}}} \tag{2}$$

where, $J = \det(F)$ is the volume ratio before and after the deformation.

For the materials undergoing large deformations, integrating the partial and spherical expressions in the reference configuration, we can get the genetic integral equation:

$$\tau^D(t) = \tau_0^D(t) + dev\left[ \int_o^\tau \frac{\dot{G}(t)}{G(0)}\overline{F}_t^{-1}(t-t') \cdot \tau_0^D(t-t') \cdot \overline{F}_t^{-T}(t-t')dt' \right] \tag{3}$$

$$\tau^B(t) = \tau_0^B(t) + \int_o^\tau \frac{K(t)}{K(0)} \cdot \tau_0^D(t-t')dt' \tag{4}$$

$$dev\left[ \int_o^\tau \frac{\dot{G}(t)}{G(0)}\overline{F}_t^{-1}(t-t') \cdot \tau_0^D(t-t') \cdot \overline{F}_t^{-T}(t-t')dt' \right] = \int_o^\tau \frac{\dot{G}(t)}{G(0)}\overline{F}_t^{-1}(t-t') \cdot \tau_0^D(t-t') \cdot \overline{F}_t^{-T}(t-t')dt' - \frac{1}{3}\left( \int_o^\tau \frac{\dot{G}(t)}{G(0)}\overline{F}_t^{-1}(t-t') \cdot \tau_0^D(t-t') \cdot \overline{F}_t^{-T}(t-t')dt' \right) : I \tag{5}$$

bending at the initial stage of loading respectively. When the sufficient load for yielding is reached, the deflection increases gradually until it loses the support. Due to the adequate toughness of the bioinspired tracheal scaffolds, the current configurations are not broken, but just lost the stability. There is no significant difference between the results of the two bioinspired tracheal scaffolds structures. Analysis of experimental data demonstrated that the bioinspired tracheal scaffolds do not only possess the moment resisting ability, but also have certain toughness around body temperature.

In order to investigate its supporting performance, the radial strength of the tracheal scaffolds has been tested by using the ZWICK-

The viscoelastic stress response σ of SMP is divided into two parts: the stress part $\sigma_0(\varepsilon)$ that is dependent on strain and the relaxation part $g(t)$ that is dependent on time. And it is

$$\sigma(\varepsilon, t) = \sigma_0(\varepsilon) \cdot g(t) \tag{6}$$

in which the hyperelastic Neo-Hooke model is used to describe $\sigma_0(\varepsilon)$. $G_0$ and $K_0$ are instantaneous shear modulus and instantaneous volume modulus respectively. In addition $G(t)$ and $K(t)$ are time-dependent shear modulus and relaxation modulus respectively. In viscoelastic constitutive model, the modulus is represented by the Prony series:

$$G(t) = G_0 \left( g_\infty + \sum_{1=1}^{n} g_i \exp \left( \frac{-t}{\tau_i} \right) \right) \qquad (7)$$

$$K(t) = K_0 \left( k_\infty + \sum_{1=1}^{n} k_i \exp \left( \frac{-t}{\tau_i} \right) \right) \qquad (8)$$

where, $g_\infty$, $g_i$, $k_\infty$ and $k_i$ are dimensionless constants. And $\sigma_0(\varepsilon)$ represents the stress-strain relation in the initial moment and $g_\infty \sigma_0(\varepsilon)$ represents the stress-strain relation when the relaxation modulus reached to an equilibrium state.

The relaxation moduli at different temperatures are required when the viscoelastic analysis involves temperature change. Based on the stress relaxation test results illustrated in Fig. 10, the modulus variations with time can be obtained by using time-temperature equivalence principle, and it can be expressed as:

$$E(T_1, t) = E \left( T_2, \frac{t}{a_T} \right) = E(T_0, \log t - \log a_T) \qquad (9)$$

This formula shows that the effect of temperature change is equivalent to the time scale divided by the shift factor $a_T$. Accordingly, $a_T$ is a function of temperature, and the WLF equation is adopted to describe that relation [41]:

$$\frac{1}{\log a_T} = -\frac{1}{C_1} - \frac{C_2}{C_1(T - T_r)} \qquad (10)$$

## 5. Results

### 5.1. Predictions on the shape memory behaviors

Combined with WLF time-temperature equivalent equation, the general Maxwell model is adopted to simulate the deformable process of the bioinspired tracheal scaffold. The bioinspired tracheal scaffold models illustrated in Fig. 12 have been established by using the Solidworks software package, which were then imported into commercial software ABAQUS (version 2016) for simulation. The bioinspired tracheal scaffold BTS-I has been meshed with 36551 quadratic tetrahedron elements (C3D10) and 503 solid 8-node quadrilateral brick elements (C3D8R). And the bioinspired tracheal scaffold BTS-II has been meshed with 28509 quadratic tetrahedron elements (C3D10) and 503 solid 8-node quadrilateral brick elements (C3D8R).

In this work, Neo-Hooke model was adopted to describe the deformation behavior at high temperature. And the time domain viscoelasticity defined by a Prony series combined with the WLF equation was utilized to describe the deformation behavior in viscoelastic state. The related parameters are given in Table 1. The obtained stress relaxation data was input as the shear test data in the ABAQUS viscoelastic material module. By normalizing the relaxation test curves shown in Fig. 10, it can be obtained three curves describing material relaxation at the temperatures of 30, 35 and 40 °C. The relaxation data obtained were fitted with the KWW function. Appendix B summarized the fitting parameters of relaxation test data. And the whole thermo-mechanical cycle process simulations are shown in Appendix C.

The initial boundary conditions of bioinspired tracheal scaffold are: $U_{x|\theta=0} = 0$, $U_{y|\theta=0} = 0$, $U_{z|\theta=0} = 0$, $\theta_{x|\theta=0} = 0$, $\theta_{y|\theta=0} = 0$ and $\theta_{z|\theta=0} = 0$, and the boundary conditions in first Visco-step are: $U_{x|\theta=0.14} = 0$, $U_{y|\theta=0.14} = 0$, $U_{z|\theta=0.14} = 0$, $\theta_{x|\theta=0.14} = 0$, $\theta_{y|\theta=0.14} = 0$ and $\theta_{z|\theta=0.14} = 6$.

### 5.2. Function verification of bioinspired tracheal scaffold in vitro

Magnetic actuation is an indirect heat-driven approach where the SMP is incorporated with a magnetic material and the SMP composite is exposed to an alternating magnetic field. Utilizing the heat generated by the oscillation of magnetic particles, the shape memory process is realized. This driving method enables the remote and non-contact control of

the actuation, which is regarded as the most elegant approach in biomedical applications [42]. And the use of medically safe magnetic fields to selectively heat thermos-regulated SMPC has been demonstrated in a number of studies [43–47]. Besides, the work of Hideo Tamai et al. demonstrated the feasibility and safety of coronary biodegradable PLA stents in humans [48]. Besides, Biological function test of shape memory PLA/Fe$_3$O$_4$ composite is shown in Appendix D. Thus with further optimization of PLA/Fe$_3$O$_4$, it may provide an effective means of deployment of tracheal scaffold.

The functional verification of bioinspired tracheal scaffolds in vitro is accomplished under the stimulus of an alternating magnetic field. Fig. 13 exhibits a set of photographs showing the shape recovery in 35 s exposed to 30 kHz alternating magnetic field. Once the scaffold was exposed to the 30 kHz alternating magnetic field, the field intensity is 4 kAm$^{-1}$. First, the scaffolds were expanded into a predetermined shape for easy process around the trachea. Then the magnetic field was imposed and the scaffolds were gradually recovered to their initial shape with time. Interestingly, both bioinspired tracheal scaffolds have been shown almost full shape recovery in 30 s. However, to ensure the best fit of the configuration of the bioinspired tracheal scaffolds to the geometry of trachea, the last 5s are necessary. The infrared camera was adopted to obtain the temperature of the structure at 35th second, and the tested temperature was 65 °C (Appendix F).

## 6. Conclusion

This paper proposes a novel fabrication method and concept for personalized customization of irregular shaped tracheal scaffolds. Two bioinspired scaffolds are fabricated through 4D printing of shape memory PLA/Fe$_3$O$_4$ composite. The developed scaffolds can be implanted in the body in a temporarily deformed configuration and deployed back into a conformed shape by exposing to an alternating magnetic field. Compared with conventional scaffolds, shape memory property of the bioinspired scaffolds helps to match the geometry of the trachea and exhibit better supporting and fixation. Besides, 4D printing technology made the morphology and microstructure of the scaffold regular and reproducible.

In addition, mechanical properties of the personally customized bioinspired tracheal scaffolds are characterized by a series of tests. The experimental results revealed that both scaffolds have high toughness, which can make them deform with the trachea deformation. Meanwhile, without loss of rigidity, the scaffold can provide reliable support for the trachea. Subjected to an alternating magnetic field, both scaffolds have been recovered to its initial shape in 35s, which indicates the successful verification of in vitro function.

## Appendix A. Supplementary data

Supplementary data to this article can be found online at https://doi.org/10.1016/j.compscitech.2019.107866.

## References

[1] S. Haykal, M. Salna, T.K. Waddell, S.O. Hofer, Advances in tracheal reconstruction, Plast. Reconstr. Surg. 2 (7) (2014) e178.
[2] M. Zarek, N. Mansour, S. Shapira, D. Cohn, 4d printing of shape memory-based personalized endoluminal medical devices, Macromol. Rapid Commun. 38 (2) (2017) 1600628.

[3] S.D. Murgu, H.G. Colt, Tracheobronchomalacia and excessive dynamic airway collapse, Respirology 11 (2006) 388–406.

[4] R. Boogaard, S.H. Huijsmans, M.W. Pijnenburg, Tracheomalacia and bronchomalacia in children: incidence and patient characteristics, Chest 128 (5) (2005) 3391–3397.

[5] A.D. Dikina, H.A. Strobel, B.P. Lai, M.W. Rolle, E. Alsberg, Engineered cartilaginous tubes for tracheal tissue replacement via self-assembly and fusion of human mesenchymal stem cell constructs, Biomaterials 52 (2015) 452–462.

[6] T. Daisuke, M. Keitaro, T. Tomoshi, M. Ryusuke, Scaffold-free trachea regeneration by tissue engineering with bio-3D printing, Interact Cardiov Th (2018) 1–8.

[7] I. Hysi, E. Kipnis, P. Fayoux, M.C. Copin, C. Zawadzki, R. Jashari, Successful orthotopic transplantation of short tracheal segments without immunosuppressive therapy, Eur. J. Cardiothorac. Surg. 47 (2015) 54–61.

[8] V. Goyal, I.B. Masters, A.B. Chang, Interventions for primary (intrinsic) tracheomalacia in children, Cochrane. Db. Syst. Rev. 10 (2012) CD005304.

[9] R.J. Morrison, S.J. Hollister, M.F. Niedner, M.G. Mahani, A.H. Park, D.K. Mehta, R.G. Ohye, G.E. Green, Mitigation of tracheobronchomalacia with 3D-printed personalized medical devices in pediatric patients, Sci. Transl. Med. 7 (2015) 287er4.

[10] L.J. Huang, L. Wang, J.K. He, J.B. Zhao, et al., Tracheal suspension by using 3-dimensional printed personalized scaffold in a patient with tracheomalacia, J. Thorac. Dis. 8 (11) (2016) 3323–3328.

[11] H. Osada, H. Tsukada, Experimental study of a new tracheal prosthesis: pored Dacron tube, J. Thorac. Cardiovasc. Surg. 127 (3) (2004) 877–884.

[12] E.P. Valerie, A.C. Durrant, V. Forte, P. Wales, et al., A decade of using intraluminal tracheal/bronchial stents in the management of tracheomalacia and/or bronchomalacia: is it better than aortopexy? J. Pediatr. Surg. 40 (6) (2005) 904–907.

[13] Y.J. Liu, H.B. Lv, X. Lan, J.S. Leng, S.Y. Du, Review of electro-active shape memory polymer composite, Compos. Sci. Technol. 69 (13) (2009) 2064–2068.

[14] H.Y. Jiang, S. Kelch, A. Lendlein, Polymers move in response to light, Adv. Mater. 18 (11) (2006) 1471–1475.

[15] F.H. Zhang, Z.C. Zhang, C.J. Luo, I.T. Lin, et al., Remote, fast actuation of programmable multiple shape memory composites by magnetic fields, J. Mater. Chem. C 3 (43) (2015) 11290–11293.

[16] W.M. Huang, B. Yang, L. An, C. Li, Y.S. Chan, Water-driven programmable polyurethane shape memory polymer: demonstrate and mechanism, Appl. Phys. Lett. 86 (11) (2005) 114105.

[17] K. Wang, G.M. Zhu, Y.K. Wang, F. Ren, Thermal and shape memory properties of cyanate/polybutadiene epoxy/polysebacic, J. Appl. Polym. Sci. 132 (23) (2015) 42045.

[18] F.H. Zhang, T.Y. Zhou, Y.J. Liu, J.S. Leng, Microwave synthesis and actuation of shape memory polycaprolactone foams with high speed, Sci. Rep. 5 (2015) 11152.

[19] J.S. Leng, X. Lan, Y.J. Liu, S.Y. Du, Shape memory polymers and their composites: stimulus methods and applications, Prog. Mater. Sci. 56 (2011) 1077–1135.

[20] O. Soykasap, Deployment analysis of self-deployable composite boom, Compos. Struct. 89 (2009) 374–381.

[21] R.R. Zhang, X.G. Guo, Y.J. Liu, J.S. Leng, Theoretical analysis and experiments of a space deployable truss, Compos. Struct. 112 (2014) 226–230.

[22] T. Xie, Tunable polymer multi-shape memory effect, Nature 464 (2010) 267–270.

[23] S.J. Varlese, L.R. Hardaway, Laminated electroformed shape memory composite for deployable light weight optics, Proc. SPIE: Earth Observing Syst IX 5542 (2004) 375–383.

[24] H.M. Wache, D.J. Tartakowska, A. Hentrich, M.H. Wagner, Development of a polymer stent with shape memory effect as a drug delivery system, J. Mater. Sci. Mater. Med. 14 (2003) 109–112.

[25] W. Zhao, L.W. Liu, X. Lan, B. Su, et al., Adaptive repair device concept with shape memory polymer, Smart Mater. Struct. 26 (2) (2017), 025027.

[26] An Jia, Chee Kai Chua, An engineering perspective on 3D printed personalized scaffolds for tracheal suspension technique, J. Thorac. Dis. 8 (2016) E1723–E1725.

[27] Y. Zhang, Post-printing surface modification and functionalization of 3D-printed biomedical device, Int. J. Bioprint. 3 (2017) 93–99.

[28] F. Pati, J. Jang, D. H Ha, D.H. Ha, S.W. Kim, et al., Printing three-dimensional tissue analogues with decellularized extracellular matrix bioink, Nat. Commun. 5 (2014) 3935.

[29] S.H. Park, T.G. Kim, H.C. Kim, et al., Development of dual scale scaffolds via direct polymer melt deposition and electrospinning for applications in tissue regeneration, Acta Biomater. 4 (5) (2008) 1198–1207.

[30] B. Leukers, H. Gulkan, S.H. Irsen, et al., Hydroxyapatite scaffolds for bone tissue engineering made by 3D printing, J. Mater. Sci. Mater. Med. 16 (2005) 1121–1124.

[31] H.Q. Wei, Q.W. Zhang, Y.T. Yao, L.W. Liu, Y.J. Liu, J.S. Leng, Direct-write fabrication of 4D active shape-changing structures based on a shape memory polymer and its nanocomposite, ACS Appl. Mater. Interfaces 9 (1) (2017) 876–883.

[32] W. Zhang, F.H. Zhang, X. Lan, J.S. Leng, et al., Shape memory behavior and recovery force of 4D printed textile functional composites, Compos. Sci. Technol. 160 (2018) 224–230.

[33] J. Aizenberg, G. Hendler, Designing efficient microlens arrays: lessons from nature, J. Mater. Chem. 14 (14) (2004) 2066–2072.

[34] P.Y. Chen, J. McKittrick, Marc André Meyers, Biological materials: functional adaptations and bioinspired designs, Prog. Mater. Sci. 57 (2012) 1492–1704.

[35] M.E. Launey, M.J. Buehler, R.O. Ritchie, On the mechanistic origins of toughness in bone, J. Mater. Res. 40 (40) (2010) 25–53.

[36] J. Nguyen, S.I. Park, D. Rosen, Heuristic optimization method for cellular structure design of light weight components, Int. J. Precis. Eng. Manuf. 14 (6) (2013) 1071–1078.

[37] A.V. Srinivasan, G.K. Haritos, F.L. Hedberg, Biomimetics: advancing man-made materials through guidance from nature, Appl. Mech. Rev. 44 (1991) 463–482.

[38] A.M. Kushner, Z. Guan, Modular design in natural and biomimetic soft materials, Angew Chem. Int. Ed. Engl. 50 (2011) 9026–9057.

[39] J. Aizenberg, V.C. Sundar, A.D. Yablon, J.C. Weaver, G. Chen, Biological glass fibers: correlation between optical and structural properties, P. Natl. A. Sci. 101 (10) (2004) 3358–3363.

[40] J. Aizenberg, J.C. Weaver, M.S. Thanawala, et al., Skeleton of euplectella sp.: structural hierarchy from the nanoscale to the macroscale, Science 309 (5732) (2005) 275–278.

[41] M.L. Williams, R.F. Landel, J.D. Ferry, The temperature dependence of relaxation mechanisms in amorphous polymers and other glass-forming liquids, J. Am. Chem. Soc. 77 (14) (1955) 3701–3707.

[42] P.R. Buckley, G.H. McKinley, T.S. Wilson, et al., Inductively heated shape memory polymer for the magnetic actuation of medical devices, IEEE Trans. Biomed. Eng. 53 (2006) 2075–2083.

[43] P. Stauffer, T. Cetas, A. Fletcher, et al., Observations on the use of ferromagnetic implants for inducing hyperthermia, IEEE Trans. Biomed. Eng. 31 (1984) 76–90.

[44] T.C. Cetas, E.J. Gross, Y. Contractor, A ferrite core/metallic sheath thermoseed for interstitial thermal therapies, IEEE Trans. Biomed. Eng. 45 (1) (1998) 68–77.

[45] A. Jordan, P. Wust, H. Fahling, W. John, A. Hinz, R. Felix, Inductive heating of ferrimagnetic particles and magnetic fluids: physical evaluation of their potential for hyperthermia, Int. J. Hyperth 9 (1993) 51–68. The Official J. Eur. Soc. Hyperthermic Oncology, North American Hyperthermia Group.

[46] W. Atkinson, I. Brezovich, D. Chakraborty, Useable frequencies in hyperthermia with thermal seeds, IEEE Trans. Biomed. Eng. 31 (1984) 70–75.

[47] N. Ramachandran, K. Mazuruk, Magnetic microspheres and tissue model studies for therapeutic applications, transport phenomena in microgravity, Ann. N. Y. Acad. Sci. 1027 (2004) 99–109.

[48] Hideo Tamai, Keiji Igaki, Eisho Kyo, Kunihiko Kosuga, et al., Initial and 6-month results of biodegradable poly-l-lactic acid coronary stents in humans, Circulation 102 (2000) 399–404.